Applied Catalysis B: Environmental 244 (2019) 262–271

Contents lists available at ScienceDirect

Applied Catalysis B: Environmental

journal homepage: www.elsevier.com/locate/apcatb

Hydroxyl decorated g-C_3N_4 nanoparticles with narrowed bandgap for high efficient photocatalyst design

Lijing Wang[a,1], Gang Zhou[d,1], Yu Tian[a], Likai Yan[a], Mingxiao Deng[a], Bai Yang[c,*], Zhenhui Kang[b,*], Haizhu Sun[a,*]

[a] College of Chemistry, National & Local United Engineering Laboratory for Power Batteries, Northeast Normal University, Changchun 130024, PR China
[b] Institute of Functional Nano&Soft Materials (FUNSOM), Jiangsu Key Laboratory for Carbon-Based Functional Materials & Devices, Soochow University, 199 Ren'ai Road, Suzhou, 215123, Jiangsu, PR China
[c] State Key Laboratory of Supramolecular Structure and Materials, College of Chemistry, Jilin University, Changchun 130012, PR China
[d] Key Laboratory of Modern Acoustics, MOE, Institute of Acoustics and Collaborative Innovation Center of Advanced Microstructures, National Laboratory of Solid State Microstructures, Nanjing University, 22 Hankou Road, Nanjing 210093, PR China

ARTICLE INFO

Keywords:
g-C_3N_4 NPs
Narrowed bandgap
Hydroxyl
Photocatalysis
Hydrogen

ABSTRACT

Zero-dimensional graphitic carbon nitride nanoparticles (0D g-C_3N_4 NPs) possess the advantages of non-toxicity, metal-free, and rich surface catalytic active sites. However, the complex preparation process, wide bandgap structure, easily particle aggregation and rapid carriers' recombination still limit their development in photocatalysis. Herein, these issues are addressed by synthesizing a novel hydroxyl (-OH) modified g-C_3N_4 NPs with a simple hydrothermal method without using any etching agents. Besides the high hydrophily and small particle size, the −OH decorated 0D g-C_3N_4 NPs possess obvious narrowed bandgap and high reduction potential. To further improve their dispersity and carriers' separation rate, 0D/3D g-C_3N_4 NPs/ZnS type II heterojunction is fabricated, which simultaneously improves the hydrophily, passivates the surface defects and extends the sunlight absorption range of ZnS. As a result, a high and cyclable photocatalytic activity of 112 μmol h^{-1} (5.6 mmol h^{-1} g^{-1}) is achieved under visible light irradiation without any co-catalysts, which is 140 times higher than that of pure ZnS and much better than the pure 0D g-C_3N_4 NPs. A systematic study of photocatalytic mechanism is proposed by combining the theoretical calculations and experimental results. This work offers a new sight for the design of 0D g-C_3N_4 NPs based photocatalysts for H_2 production.

1. Introduction

As an economically feasible strategy to address the growing energy crisis, photocatalytic hydrogen technology has attracted increasing attention, which can transform sustainable solar energy into clean and carbon-free fuel [1–6]. An ideal photocatalyst should simultaneously contain the virtues of suitable bandgap, proper hydrophily, large surface area to make the photocatalytic reaction feasible, and as cost-effective as possible for industrial production. With the advantages of non-toxic, metal-free and earth-abundant characters, graphitic carbon nitride (g-C_3N_4) shows great promising as the next generation photocatalyst for hydrogen production [7–10]. However, the poor hydrophily, low surface area and wide bandgap restrict the photocatalytic activity of pristine g-C_3N_4.

Many efforts have been made to address these issues [11,12], among which the reduction of dimension is widely used to improve the hydrophily and increase the surface area of g-C_3N_4 [13]. Moreover, lower dimension g-C_3N_4 nanomaterials, especially zero dimension g-C_3N_4 nanoparticles (0D g-C_3N_4 NPs), usually exhibit shorter charge-transfer length and have rich surface catalytic active sites such as edge amine groups and hydroxyl radical for hydrogen evolution [14–16]. For example, Wang et al. prepared g-C_3N_4 quantum dots/bulk g-C_3N_4 (BCN) photocatalyst via a thermal-chemical etching process. A desired high hydrogen evolution rate (HER) was achieved with Pt as co-catalyst [9,17], indicating the great potential of g-C_3N_4 nanomaterials in the field of photocatalysis. However, the present synthetic approaches for 0D g-C_3N_4 NPs usually involve in complex oxidation-reduction reactions and tedious cleaning process, which are time-consuming and low yields. Besides, the reported 0D g-C_3N_4 NPs often possess wider bandgap compared to the 2D or 3D g-C_3N_4 materials due to their

* Corresponding authors.
E-mail addresses: byangchem@jlu.edu.cn (B. Yang), zhkang@suda.edu.cn (Z. Kang), sunhz335@nenu.edu.cn (H. Sun).
[1] These authors contributed equally to this work.

https://doi.org/10.1016/j.apcatb.2018.11.054
Received 25 September 2018; Received in revised form 9 November 2018; Accepted 18 November 2018
Available online 19 November 2018
0926-3373/ © 2018 Elsevier B.V. All rights reserved.

quantum size effect, resulting in lower utilization of visible light. Moreover, high costly noble metal co-catalysts (e.g., Pt) are always required during the photocatalytic process [17], which limits their practical applications. In addition, a systematic study of photocatalytic mechanism is seldom reported owing to the unclear structure of the existing 0D g-C_3N_4 NPs. Therefore, it is still a challenge to develop a simple approach to prepare small sized g-C_3N_4 NPs with narrower bandgap, and explore its surface structure to fully study the possible photocatalytic mechanism for hydrogen production, especially under the case of noble metal free.

Recently, oxygen containing functional groups are regarded as the reaction active site of photocatalysis [18,19]. A proper O doping may narrow the bandgap and improve the hydrophily of catalysts at the same time [6]. Inspired by this idea, herein, hydroxyl (-OH) is selected to replace amino (-NH_2) on the surface of g-C_3N_4 NPs via a simple hydrothermal method without the assistance of any etching reagents. Especially, the reduced dimension, narrowed bandgap, increased surface area and better hydrophily are simultaneously achieved. Moreover, the high reduction potential is well reserved for hydrogen production even if the bandgap is narrowed. To improve their dispersity and carriers' separation rate, a unique structure is then developed that 0D g-C_3N_4 NPs are anchored onto the surface of 3D ZnS microstructure to form ZCN-X composites (X = 1, 2, 3, refers to the feed molar ratio of g-C_3N_4 to ZnS). The hydroxyl decorated g-C_3N_4 NPs improve the hydrophily, passivate the surface Zn defects and extend the sunlight absorption range of ZnS. Their respective carriers' separation ability are simultaneously improved by building type II heterojunction. As a result, a high and recyclable photocatalytic hydrogen production activity of 112 μmol h^{-1} (5.6 mmol h^{-1} g^{-1}) is achieved by ZCN-2 composite under visible light without any co-catalyst, which is 140 times higher than that of pure ZnS, and much better than that of pure g-C_3N_4 NPs [6,9,10,20]. A systematic study of photocatalytic mechanism is proposed by combining the theoretical calculations and the experimental results.

2. Experimental details

2.1. Synthesis of bulk g-C_3N_4 (BCN) and g-C_3N_4 NPs

BCN was prepared by heating melamine for 4 h at 550 °C under Ar atmosphere. After being grinded into powder, BCN (50 mg) was dissolved in deionized water (25 mL) and treated under ultrasound for at least 60 min. To further improve the dispersion of g-C_3N_4, the mixture was stirred for at least 120 min. Then, the well dispersed BCN solution was transferred to 50 ml autoclaves and kept at 200 °C for 6–12 h. A clear and transparent g-C_3N_4 NPs solution was then obtained. Afterwards, the above solution was condensed by spin-steaming method and dialyzed for at least 24 h to remove the foreign ion during the hydrothermal reaction process. The purified NPs was further filtered through 0.22 μm polyethersulfone membrane to remove the agglomerated particles. To receive the g-C_3N_4 NPs powder, the concentrated solution was freeze-dried for at least 48 h.

2.2. Synthesis of ZnS(en)$_{0.5}$

ZnS(en)$_{0.5}$ was synthesized based on the method described in previous literature with a slight modification. First, $ZnCl_2$ (2 mmol) and thiourea (4 mmol) were added into 50 ml ethylenediamine with constant stirring. After $ZnCl_2$ and thiourea were completely dissolved, the white gelatinous product was transferred into a 100 ml Teflon-lined autoclave and kept at 180 °C for 18 h, washed with deionized water and absolute ethyl alcohol several times, and then dried for further experiment.

2.3. Synthesis of ZCN-X microstructure

ZCN-X was prepared using ZnS(en)$_{0.5}$ and BCN powder as precursors. First, ZnS(en)$_{0.5}$ (60 mg) nanosheets and different amount of BCN powder (0, 60, 120, and 180 mg) were mixed and dispersed in 50 ml deionized water under ultrasound for about 60 min, followed by constantly stirring for at least 120 min. Then, the above mixture was transferred into autoclaves and kept at 200 °C for 12 h. The above solution was transferred to a dialysis bag and dialyzed for at least 24 h to remove the foreign ion during the hydrothermal reaction process. Finally, the obtained products were centrifuged and dried into powder for further characterization.

2.4. Photocatalytic H_2 production activity measurement

The photocatalytic hydrogen evolution activities of photocatalyst were tested by using a photocatalytic activity evaluation system (CEL-SPH2N). The light source was a 300 W Xe lamp with/without a light cutoff at 420 nm. photocatalyst powder (20 mg) was directly dispersed into 50 ml of the Na_2S (0.25 M) and Na_2SO_3 (0.35 M) mixture solution. Before irradiation, the whole system was sealed and vacuumed by a mechanical pump to eliminate any gas impurities. Then, the produced hydrogen was extracted every 30 min with an on-line gas chromatograph for seven times. The generated amount of hydrogen was evaluated according to the fitted standard curve. The average quantum efficiency (QE) of different photocatalysts were obtained according to Equation (1):

$$\mathrm{QE}(\%) = \frac{2 \times \text{number of evolved H2 molecules}}{\text{number of incident photons}} \times 100 = \frac{2\mathrm{nNAhc}}{\mathrm{PS}\lambda\mathrm{t}} \times 100 \quad (1)$$

where n is the evolution amount of H_2, N_A (6.022×10^{23} mol^{-1}) is Avogadro's constant, h (6.626×10^{-34} J s) is Planck's constant, c (2.998×108 m s^{-1}) is the speed of light, λ (420×10^{-9} m) is the wavelength of the incident light, P (35.5 W m^{-2}) is the power density, S (1.9625×10^{-3} m^2) is the irradiation area, and t (3600 s) is the irradiation time.

2.5. Characterization

Powder X-ray diffraction patterns (XRD) were obtained using a Shimadzu XRD-6000 diffraction system. A Nicolet AVATAR 360 FT-IR spectrophotometer was used to achieve the Fourier transform infrared (FT-IR) spectrum. Transmission electron microscopy (TEM) was performed on a JEOL 2010 at an accelerating voltage of 200 kV. X-ray photoelectron spectrometry (XPS) was conducted on a VG ESCALAB MKII spectrometer. UV–vis absorption spectra were obtained using a Shimadzu 3600 UV–vis-NIR spectrophotometer. PL spectra and fluorescence decay curves of the catalyst powder were studied with RF-5301PC and FLS980 equipment. Nitrogen adsorption-desorption (BET) isotherms were examined using an autosorb-IQ instrument (TriStar II3020 of America). Ultraviolet photoelectron spectroscopy (UPS) was performed on a VG Scienta R3000 analyzer in ultrahigh vacuum with a base pressure of 1×10^{-10} mbar. To acquire the contact angle measurements, a commercial contact angle system (DataPhysics, OCA 20) was used with 3 μL of water droplet as the indicator. Element analysis (EA) was obtained using the instrument of EA3000, and inductively coupled plasma mass spectrometry (ICP) was operated on Agilent 725 system with the concentration of ppm level. The Solid-state 13C MAS NMR spectra is conducted on a Bruker AV III 400 WB instrument.

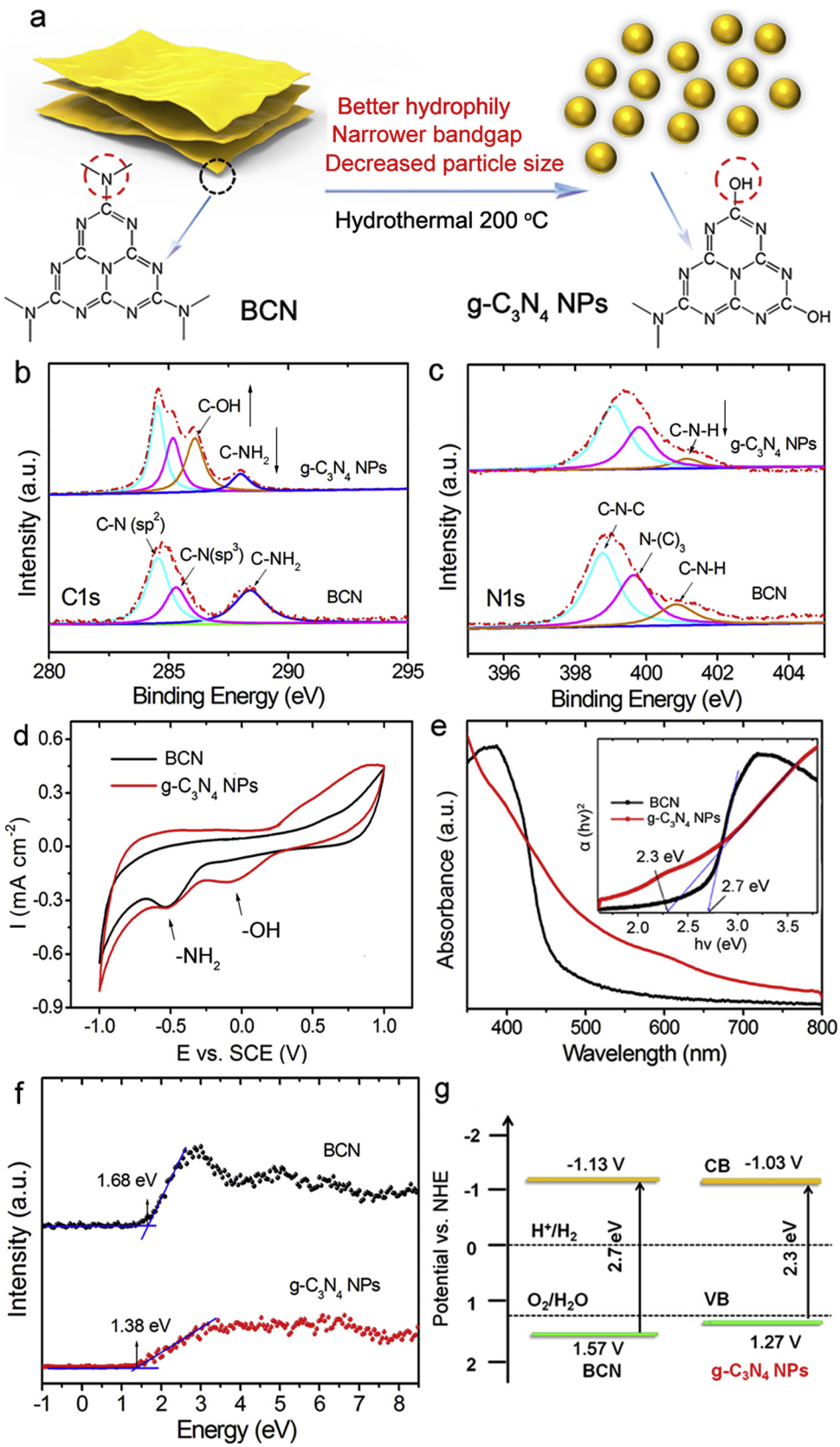

Fig. 1. (a) Possible reaction scheme: the change from BCN to g-C_3N_4 NPs during the hydrothermal treatment; High resolution XPS spectra of (b) C1 s and (c) N1 s of BCN and g-C_3N_4 NPs; (d) CV curves of BCN and g-C_3N_4 NPs, indicating the co-existance of -NH_2 and -OH − OH groups in g-C_3N_4 NPs; (e) UV–vis absorption and bandgap structures of BCN and g-C_3N_4 NPs powder, indicating the narrower bandgap of g-C_3N_4 NPs than BCN; (f) XPS valence band spectra of BCN and g-C_3N_4 NPs; (g) Band structure alignments of BCN and g-C_3N_4 NPs, indicating the reserved high reduction potential of g-C_3N_4 NPs.

3. Results and discussion

3.1. Composition and chemical states

As shown in Fig. 1a and Fig. S1, g-C_3N_4 NPs are directly synthesized using a simple hydrothermal method from the micron bulk g-C_3N_4 (BCN) [21]. The results of element analysis (EA), inductively coupled plasma mass spectrometry (ICP) in Table S1, and X-ray photoelectron spectroscopy (XPS) in Fig. S2a simultaneously show that g-C_3N_4 NPs exhibit increased oxygen content (from 2.2 to 25.4 mol.%) and decreased nitrogen content (from 63.5 to 21.3 mol.%) compared with BCN, indicating the formation of oxygen-containing groups. Besides, compared to BCN, the C 1 s peak of g-C_3N_4 NPs shifts to lower binding energy, while the N 1 s shifts to higher binding energy in the XPS spectra. Generally, the binding energy of C and N element are closely related to their chemical environment and valence states [22–24]. In comparison with BCN, the introduction of C—O band changed the chemical environment of C and N element in g-C_3N_4 sample, which results in the peak displacement in the XPS spectra of g-C_3N_4 NPs [6,17]. In addition, according to the Fourier transform infrared (FT-IR) spectroscopy in Fig. S2b, the absorption band located at 813 cm^{-1} originated from the characteristic bending vibration of triazine ring is well reserved in g-C_3N_4 NPs, indicating that the change might occur in the ending group rather than the ring framework. Besides, the weakened intensity stretching vibration signal at around 1744 cm^{-1} demonstrates decreased C—N bonds, while the wider stretching vibration signal between 3085 and 3300 cm^{-1} indicates more C—OH bonds exist on the surface of g-C_3N_4 NPs than BCN [25]. Therefore, a possible structure change is proposed in Fig. 1a, where the surface -NH_2 are substituted by —OH group.

In the C1 s spectra of g-C_3N_4 NPs and BCN (Fig. 1b), apart from the typical peaks at 284.5 [C—N (sp^2)], 285.3 [C—N (sp^3)], and 288.4 eV [C—NH_2], an additional peak at 286.1 eV that corresponds to C—OH is observed [13], whereas the peak intensity related to the C-NH_2 bond at 288.4 eV, as well as the peak at 400.8 eV (C—N—H) in the high resolution N1 s XPS spectrum of g-C_3N_4 NPs are obviously decreased (Fig. 1c), indicating most of C—NH_2 groups are replaced by C—OH groups. Moreover, in the cyclic voltammetry (CV) curves of BCN and g-C_3N_4 NPs (Fig. 1d), BCN only shows one reduction peak that is attributed to the existance of -NH_2 group [26], while an additional peak around 0 V is observed in g-C_3N_4 NPs electrode, which may be ascribed to —OH group [25]. To further confirm this point, the CV curve of amino-1, 3-propanediol containing both -NH_2 and —OH groups is shown in Fig. S3a. It is clearly observed that the peak positions of g-C_3N_4 NPs are well consistent with those of amino-1, 3-propanediol, indicating the co-existance of -NH_2 and —OH groups in g-C_3N_4 NPs. Solid-state ^{13}C magic angle spinning (MAS) NMR measurements are provided to further confirm the change of carbon related groups. As shown in Fig. S3b, NMR of BCN presents two strong peaks at 156.6 and 164.8 ppm, corresponding to the chemical shifts of C_{3N} (1) and $C_{2N\text{-}NH2}$ (2) in the heptazine units, respectively [27,28]. For g-C_3N_4 NPs, a new peak at 129.8 ppm is clearly observed, which may be ascribed to the C_{2N-OH} (3). The results of XPS spectra, CV curves and MAS NMR measurements confirm that most of the -NH_2 functional groups are transformed into —OH.

The transform of amino into hydroxyl will narrow the bandgap of g-C_3N_4 NPs, which is first proven by the theoretical calculations based on $DMol^3$ code [6]. According to the proposed structural change in Fig. S4, the highest occupied molecular orbital-lowest unoccupied molecular orbital (HOMO-LUMO, H–L) gap of BCN and g-C_3N_4 NPs are calculated and listed in Table S2, from which a trend of H—L gap narrowing is observed for hydroxyl-g-C_3N_4 NPs. This theoretical predict is in good accordance with the experimental results. From Fig. 1e, the UV spectra show that the small sized g-C_3N_4 NPs present obviously extended sunlight harvesting range and narrower bandgap (2.3 eV) than the bulk one (2.7 eV). Although the bandgap of the g-C_3N_4 NPs become narrower, the high reduction ability of g-C_3N_4 is well reserved. As shown in Fig. 1f, g-C_3N_4 NPs possess much lower VB maximum (1.38 eV) than the pristine BCN (1.68 eV) vs. vacuum level. According to the Eq. 2:

$$E_{NHE}/V = \Phi + E_{VL}/eV - 4.44 \quad (2)$$

where E_{NHE} is the potential of normal hydrogen electrode; Φ is the electron work function of the analyzer (4.30 eV), E_{VL} is the potential of vacuum level [29]. VB of g-C_3N_4 NPs and BCN is 1.24 and 1.54 V vs. NHE, respectively. In combination with the bandgap obtained from UV spectra, their conduction band (CB) are -1.03 and -1.13 V, respectively (Fig. 1g). Therefore, the narrowed bandgap of the g-C_3N_4 NPs is mainly attributed to the change of VB position rather than CB, which ensures high reduction potential of 0D g-C_3N_4 NPs as photocatalyst. In addition, the change of the functional groups and particle size is beneficial for the improvement of hydrophily and specific surface area. As shown in Fig. S5 and Fig. S6, g-C_3N_4 NPs possess larger specific surface area (from 35.6 to 68.2 $m^2\ g^{-1}$), pore size (from 3.4 to 3.8 nm), pore volume (from 0.03 to 0.12 $cm^3\ g^{-1}$) and better hydrophily (from 35° to 3°) than BCN. As far as we know, the preparation of 0D g-C_3N_4 NPs with smaller particle size, narrower bandgap, better hydrophily and high reduction potential by a simple hydrothermal method is seldom reported.

3.2. Structure and morphology

The transmission electron microscopy (TEM) image (Fig. 2a) shows that the prepared g-C_3N_4 NPs with the size less than 20 nm are well-dispersed in water solution. The lattice spacing of 0.336 nm in the high-resolution TEM (HRTEM, inset of Fig. 2a) image corresponds to the (002) plane of hexagonal g-C_3N_4. To improve the dispersion and carriers' separation ability of g-C_3N_4 NPs, 3D ZnS, with the advantages of low cost and low toxicity is introduced to form ZCN-X composites. In Fig. 2b, the TEM images of composite directly confirm the successful preparation of ZCN-2 heterojunction. Many visible and well dispersed nanoparticles less than 20 nm on the micron-hexagonal surfaces of ZnS are observed. From HRTEM images of the composites shown in Fig. 2c, the lattice spacing of 0.270 and 0.331 nm correspond to the (220) plane of wurtzite ZnS and (002) plane of hexagonal ZnS, respectively, thus a ZnS phase heterojunction is built, which is favorable to achieve high photocatalytic activity [30]. As shown in Fig. S7, compared with ZnS, the upward shift binding energy of Zn 2p in ZCN-2 is due to the interfacial interaction between ZnS and g-C_3N_4 and the existence of Zn-N bonds [31], which further proves the successful formation of heterojunction between ZnS and g-C_3N_4 NPs. In addition, we prove the thermal stability of the ZCN-X by performing the *ab initio* molecular dynamic (*AIMD*) simulation at room temperature (300 K) in a canonical ensemble (*NVT*) based on the quantum molecular dynamics. Generally, the quantum molecular dynamics describes the time-evolution of a chemical system at the atomic level by directly solving the Schrodinger equation, and the stability of the molecular structure can be judged by the changes of the molecular structure in a certain time range [32–34]. As shown in the GIF animation based on a large cell containing 267 atoms, after 6 ps with a time step of 1 fs, no distinct structural destruction of ZCN-X can be found, except for some thermal-induced fluctuations. This suggests that ZCN-X is thermally stable at room temperature. Please refer to the Video 1 (ESI†). In addition, the lattice spacing of 0.336 nm is associated with the (002) plane of hexagonal g-C_3N_4. The tight interface contact between wurtzite ZnS and hexagonal g-C_3N_4 shows the formation of high quality heterojunction structures, which will significantly improve the carriers' separation and transfer rate. These results are in good accordance with the powder X-ray diffraction (XRD) patterns of g-C_3N_4 NPs. As shown in Fig. 2d, the diffraction peaks at 13.6° and 27.3° of the red line are attributed to (100) and (002) crystal planes of g-C_3N_4 NPs. Besides, the weak intensity and broadened width of the peak may be caused by the small, thin structure and low crystallinity of g-C_3N_4 NPs [35]. The structure of ZnS contains

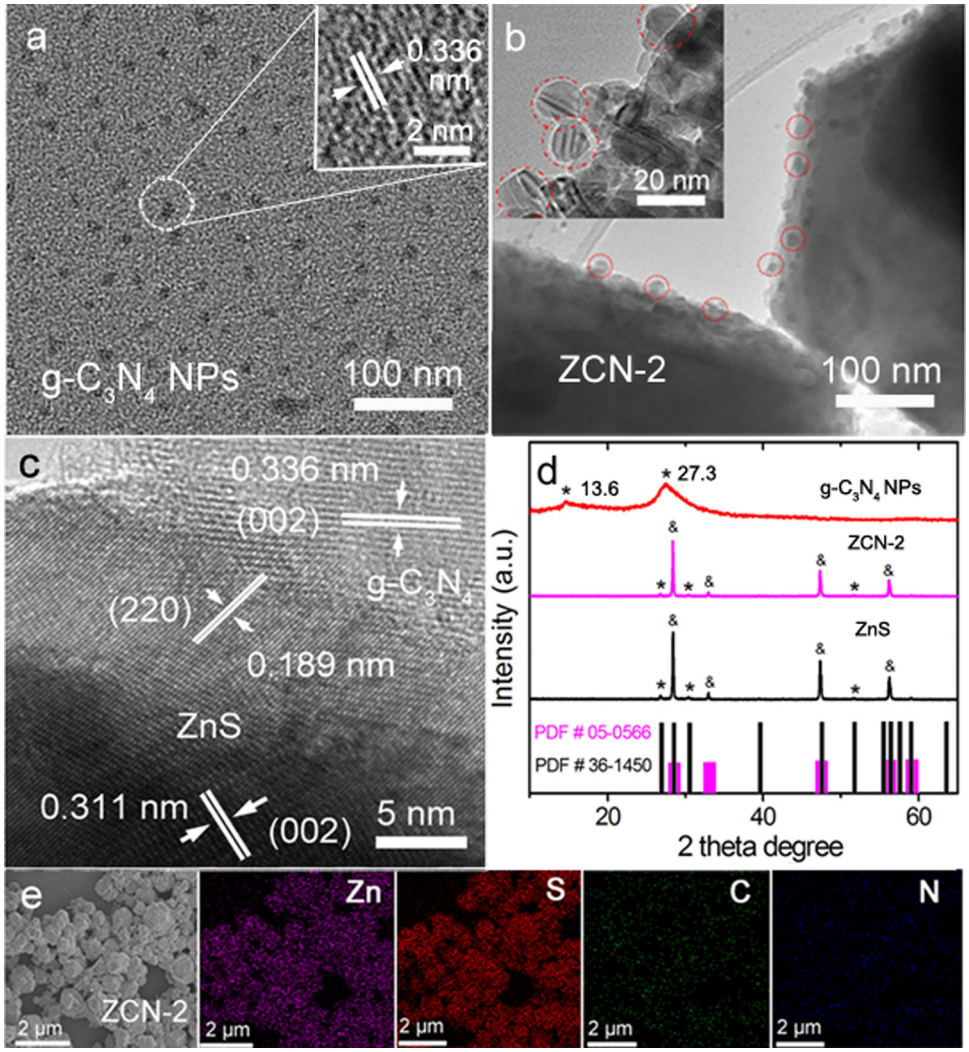

Fig. 2. TEM images of (a) g-C_3N_4 NPs and (b) ZCN-2; (c) HR-TEM image of ZCN-2; (d) XRD spectra of ZnS, g-C_3N_4 NPs and ZCN-2; (e) Mapping pictures of ZCN-2 sample, indicating the successful preparation of ZCN-2 and homogeneous distribution of Zn, S, C, and N elements.

a mixture of wurtzite (JCPDF#05-0566) and hexagonal (JCPDF#36-1450) phases. For the composites (e.g., ZCN-2), the XRD pattern is found to be consistent with that of ZnS, that is, because of the small size, low crystallinity and good dispersion of g-C_3N_4 NPs on the ZnS microstructure, the peak of g-C_3N_4 NPs cannot be obviously presented. The elemental mapping gives direct evidence that carbon and nitrogen are homogenously distributed on the ZnS microstructure (Fig. 2e), indicating the high dispersion ability of g-C_3N_4 NPs phase on the ZnS surface.

3.3. Photocatalytic performance and stability

As shown in Fig. 3 and Fig. S8, BCN has a low photocatalytic activity of 0.026 mmol h^{-1} g^{-1} resulting from the limited sunlight absorption range and small surface area, while g-C_3N_4 NPs show enhanced photocatalytic activity of 0.052 mmol h^{-1} g^{-1} than BCN based on the higher surface area, narrower bandgap and better hydrophily. The unobvious improvement in HER is owing to the easy particle self-aggregation and heavy recombination of photoexcited carriers in g-C_3N_4 NPs. As proven in Fig. S1 and Fig. 2d, g-C_3N_4 NPs possess smaller particle size than BCN, and the full width at half maximum of g-C_3N_4 NPs is much wider than BCN (Fig. S9b), indicating g-C_3N_4 NPs have much weaker crystallization and more surface defects [36]. The excessive surface defects often become the recombination center of carriers, and hence g-C_3N_4 NPs have faster recombination rate of carriers than BCN [37]. However, HER shows significant improvement once g-C_3N_4 NPs are combined with ZnS, because the heterojunction constructed between them provides a driving force to support the separation and transfer of charge carriers. As shown in Fig. 3 and Fig. S8, the HER of ZnS, ZCN-1, ZCN-2 and ZCN-3 are 0.360, 3.466, 6.800 and 4.598 mmol h^{-1} g^{-1}, respectively, their corresponding average quantum efficiency are 0.08%, 4.88%, 13.01% and 8.73% at 420 nm. ZCN-2 presents the highest photocatalytic activity and average quantum efficiency. The decreased activity of g-C_3N_4 NPs rich sample (ZCN-3) may be resulted from the following reasons: on the one hand, the excessive g-C_3N_4 NPs may agglomerate together, leading to the decrease of reaction active sites, and become the recombination center of carriers, hence reduce the carrier seperation and transfer rate; On the other hand, the redundant g-C_3N_4 NPs covered on the surface of ZnS may prevent the light absorption and carrier generation of ZnS and finally result in the decreased photocatalysis activity. In addition, significant improvement of HER is also observed for ZCN-2 even with the normalized specific surface area (Table S3), indicating that there are also other factors contribute to the improvement of photocatalytic performance except for the increase of surface area. Moreover, as shown in Fig. 3c, ZCN-2 possesses an efficient visible light photocatalytic HER of 5.6 mmol h^{-1} g^{-1}, which is 140 times higher than that obtained from ZnS and 3.8 times higher than the pristine BCN-ZnS

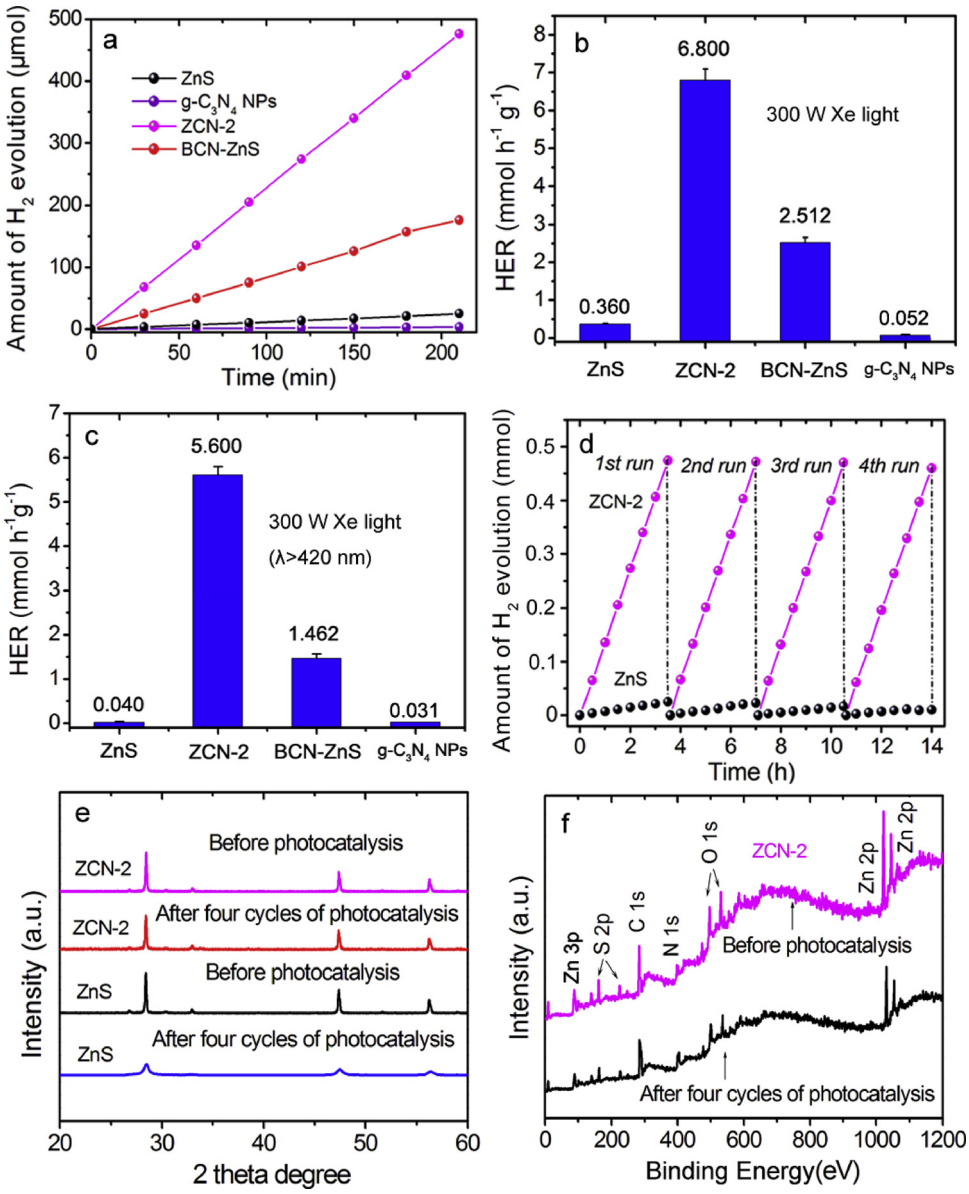

Fig. 3. (a) The photocatalytic hydrogen evolution amount of ZnS, g-C_3N_4 NPs, ZCN-2 and BCN-ZnS composite in 210 min with 20 mg photocatalysts; HER of ZnS, g-C_3N_4 NPs, ZCN-2 and BCN-ZnS composite with 0.25 M Na_2S and 0.35 M Na_2SO_3 mixed aqueous solution as a hole scavenger under (b) 300 W Xe light and (c) visible light ($\lambda > 420$ nm); (d) amount of H_2 evolution by ZnS and ZCN-2 samples for four photocatalytic cycles under 300 W Xe light; (e) XRD curves of ZnS and ZCN-2 before and after four cycles of photocatalytic cycles; (f) XPS survey spectra of ZCN-2 before and after four cycles of photocatalysis.

photocatalyst. The performance also competes with the best g-C_3N_4 and ZnS-related photocatalysts reported under similar conditions [6,9,10,30]. A comparison of this work with other current related investigations under visible light with/without Pt as co-catalyst are listed in Table S4 and Table S5, indicating the great advantages of ZCN-X photocatalyst as a clean, low toxic, and cost-effective material for hydrogen production.

The long-term stability is another important parameter of the photocatalytic performance. As shown in Fig. 3d, after four cycles of repeated trials, ZCN-2 shows negligible change in HER performance while the photocatalytic activity of ZnS gradually decreases. Moreover, after the four repeated experiments, the XRD diffraction peaks of pure ZnS become significantly weakened and widened, while the XRD and XPS spectra (Fig. 3e and f) of ZCN-2 before and after photocatalysis basically remain the same. As shown in Table S6, after four cycles of photocatalysis, there is no obvious change in C, N, Zn, S and O element content. In addition, as shown in Fig. S10, TEM images of g-C_3N_4 NPs in ZCN-2 before and after photocatalysis basically remain the same. Therefore, the amount and structure of g-C_3N_4 NPs in ZCN-2 did not show obvious change after four cycles of photocatalysis, confirming that the g-C_3N_4 NPs-modified ZnS composite is more photostable and thermostable than pure ZnS. In addition, the TEM and FTIR spectra after four cycles of test are also investigated. As shown in Fig. S10, after photocatalysis, obvious lattice can also be found for g-C_3N_4 NPs, and there is no obvious change in the FTIR spectra, indicating the fairly well photostability and thermal stability of g-C_3N_4 NPs.

4. Photocatalytic mechanism

4.1. Bandgap, specific surface area and hydrophily

A possible photocatalytic mechanism of ZCN-2 porous nanosheets are proposed. Generally, photocatalysis reaction involves the following three processes: carrier generation, migration and surface oxidation-reduction. The number of generated carriers is determined by the solar light absorption capacity of the catalyst, while the carrier transport

capacity affects the number of carriers eventually migrated to the catalyst surface to participate in the redox reaction. The hydrophily and specific surface area affect the quality of redox reaction on the photocatalyst surface. Higher hydrophily and larger specific surface area will contribute to better contact between catalyst and water, which will bring about more active sites as well as better photocatalytic activity. Firstly, ZCN-2 composite possesses extended solar light responsible range, larger surface area and better hydrophily than ZnS. As shown in Fig. S11a, ZnS possesses a significant absorption at a wavelength shorter than 365 nm on account of its wide bandgap, while an additional absorption peak at ~480 nm attributed to g-C_3N_4 NPs is found in the ZCN-2 samples, which will produce more electron-hole pairs via improved utilization of sunlight [38]. The specific surface area of ZnS and ZCN-2 are measured by the typical nitrogen adsorption and desorption isotherms (BET). As shown in Fig. S11b, all samples exhibit type IV isotherms, indicating the presence of mesopores (2–50 nm). ZnS possesses a low specific surface area of 21.5 $m^2 g^{-1}$, while an increasing surface area of 56.8 $m^2 g^{-1}$ is observed for ZCN-2 composite. This brings more active sites, enhanced sunlight utilization rate, and better contact between photocatalyst, incident light, and water during the hydrogen production process [39,40]. Moreover, the contact angle decreases from 37° to 20° because of the proper introduction of g-C_3N_4 NPs with high hydrophilic hydroxyl (Fig. 4a). This ensures better hydrophilic surface of ZCN-2 than ZnS, which is beneficial to enhance water adsorption and the proton reduction reaction for hydrogen production [6].

4.2. Separation and transport ability of carriers

As shown in Fig. S12 and Fig. S13, Zn-N bond is built between ZnS and g-C_3N_4 NPs based on the consistent bond length with literatures [41,42]. The interface electronic interaction between ZnS and g-C_3N_4 NPs brings about a high charge density, and most charges are localized at ZnS/g-C_3N_4 hybridized interface region. This mainly results from the type II heterojunction between ZnS and g-C_3N_4 NPs, which bring about charge transfer between ZnS and g-C_3N_4. Upon solar light illumination, both ZnS and g-C_3N_4 NPs capture photons with different energies to excite CB electrons and generate VB holes inside their energy bands (Scheme 1). As calculated by the combination of Kubelka-Munk method with ultraviolet photoelectron spectroscopy (UPS) spectra in Fig. S14, a type II heterojunction is created between ZnS and g-C_3N_4 NPs according to their matched bandgap structure (the detail calculation process is offered in supporting information), which will greatly improve the separation and transfer rate of carriers. The photogenerated CB electrons are collected in the CB of ZnS to initiate the hydrogen evolution reaction, whereas the photogenerated VB holes are transferred into the g-C_3N_4 NPs' VB and consumed afterwards by sacrificial agents. Then, the recombination of electron-hole pairs is retarded by the reverse transfer of positive and negative charge carriers, increasing the output and lifetime of electrons. Moreover, the ZCN-2 overcomes the readily carriers' recombination in ZnS resulting from the defect levels in it. Generally, electrons excited from VB to CB in pure ZnS are partly captured in zinc vacancy (V_{Zn}). With a lower reduction potential, they are not able to reduce water to hydrogen but will recombine with the holes. In other words, V_{Zn} acts as the recombination center of electron and hole pairs, decreasing the photocatalytic activity and stability of ZnS. Once g-C_3N_4 NPs are introduced, the electrons in V_{Zn} can be re-excited to the CB of ZnS by the specific photons from the recombination radiation of decorated g-C_3N_4 NPs [43]. Therefore, the defect site can be passivated, allowing more electrons to participate in the photocatalytic reduction reaction.

The charge-carrier transfer mechanism can be further proven by the room temperature PL spectra, transient photocurrent and electrochemical impedance spectra (EIS). As shown in Fig. 4b, both ZnS and ZCN-2 samples present two PL peaks at ~370 and 468 nm, which originate from the intrinsic near-band-edge and defect-related recombination of electron-hole pairs in ZnS, respectively. Interestingly, after the decorating of g-C_3N_4 NPs, both the defect and intrinsic emission peak intensities become weakened. The peak intensity attributed to the defect of ZCN-2 presents a more serious decrease than its intrinsic peak. From Fig. 4b, the integral peak area ratio of the intrinsic peak to the defect peak of ZCN-2 (3594/288 = 12.5) is much larger than that of ZnS (6932/1389 = 5.0), indicating the effective passivation of surface defects of ZnS. Such an anti-recombination effect is attributed to the excitation of photogenerated electrons in V_{Zn} and the carriers' transport in reverse directions between ZnS and g-C_3N_4 NPs. To acquire further insight into the mechanism for the progress of photogenerated carrier dynamics, the multidimensional time-correlated single photon counting method is adopted to evaluate the PL decay process of samples upon an excitation of 280 nm (detailed fitting data are listed in Table S7). A more noticeable prolonged lifetime with an emission wavelength of 468 nm (from 3.3 to 5.3 ns in Fig. 4c) than that of 370 nm (from 4.2 to 5.2 ns in Fig. 4d) is also observed. This proves that the recombination at the V_{Zn} site is limited due to the defect passivation of ZnS brought by g-C_3N_4 NPs, which is consistent with the results discussed above. In generally, the prolonged lifetime clearly suggests that the photoexciton dissociation is accelerated in the ZCN-2 sample, confirming the proposed spatially separation of carriers at the interface between the g-C_3N_4 NPs site and ZnS support.

The transient photocurrent of the samples is measured during repeated on/off illumination cycles at 1.0 V. As shown in Fig. 4e and Fig. S15, ZnS displays a notably low photocurrent response upon each illumination, owing to the rapid recombination of carriers, while ZCN-2 exhibits significantly enhanced reproducible photocurrent response with long-term stability of at least 5000 s due to the modification of g-C_3N_4 NPs. To obtain a more thorough understanding of the charge transfer behavior of ZCN-2 in the absence of light excitation, EIS measurements are taken under light and dark conditions, as shown in Fig. 4f. The inset is the equivalent electrical circuit simulated by the EIS Nyquist plots, where R_s and R_t represent the electrolyte solution resistance and interfacial charge-transfer resistance/electrolyte, CPE is the constant phase element, respectively [44,45]. Based on the above model, the fitting data of all samples are summarized in Table S8 (ESI†). ZCN-2 shows much smaller diameter, R_s and R_t value under the two conditions, indicating its lower resistance for interfacial charge transfer from electrode to electrolyte molecules. In addition, the lower R_s of ZCN-2 than ZnS is attributed to the smaller contact resistance at the interface between the electrolyte and the electrode [46,47]. As shown in Fig. 4a, the contact angle of ZnS decreases from 37° to 20° because of the proper introduction of g-C_3N_4 NPs with high hygrophilic hydroxyl. This ensures better hydrophilic surface of ZCN-2 than ZnS, thus ZCN-2 electrode has smaller contact resistance with electrolyte than ZnS. Combined with the above steady state and time-resolved PL spectroscopy results, it is confirmed that the enhanced photocatalytic activity and stability of ZCN-2 is mainly based on the enhanced carriers' transfer rate and effective passivation of V_{Zn} by the modification of g-C_3N_4 NPs.

4.3. Hydrogen adsorption and desorption equilibrium

Moreover, a suitable hydrogen adsorption and desorption equilibrium is also achieved in the ZCN-X system. A lower hydrogen adsorption free energies (ΔG_{H^*}) alway brings high surface coverage of H^* (atom), while a larger ΔG_{H^*} leads to H^+ bond too weakly on the surface of photocatalyst [44]. They both give rise to slow HER kinetics and therefore, an optimal photocatalytic activity will be obtained when $\Delta G_{H^*} \approx 0$. From Scheme 1b, density-functional theory (DFT) calculation indicates that the ZCN-X heterojunction introduces a non-equilibrium stoichiometry to allow a favorable hydrogen adsorption as follows: $H^+ + e^- + {}^* \rightarrow H^*$, which contributes to improved photocatalytic hydrogen production activity.

This work shows that the change of surface functional group of g-C_3N_4 NPs via a simple hydrothermal method. It is expected that besides −OH, there are much more other functional groups, for example,

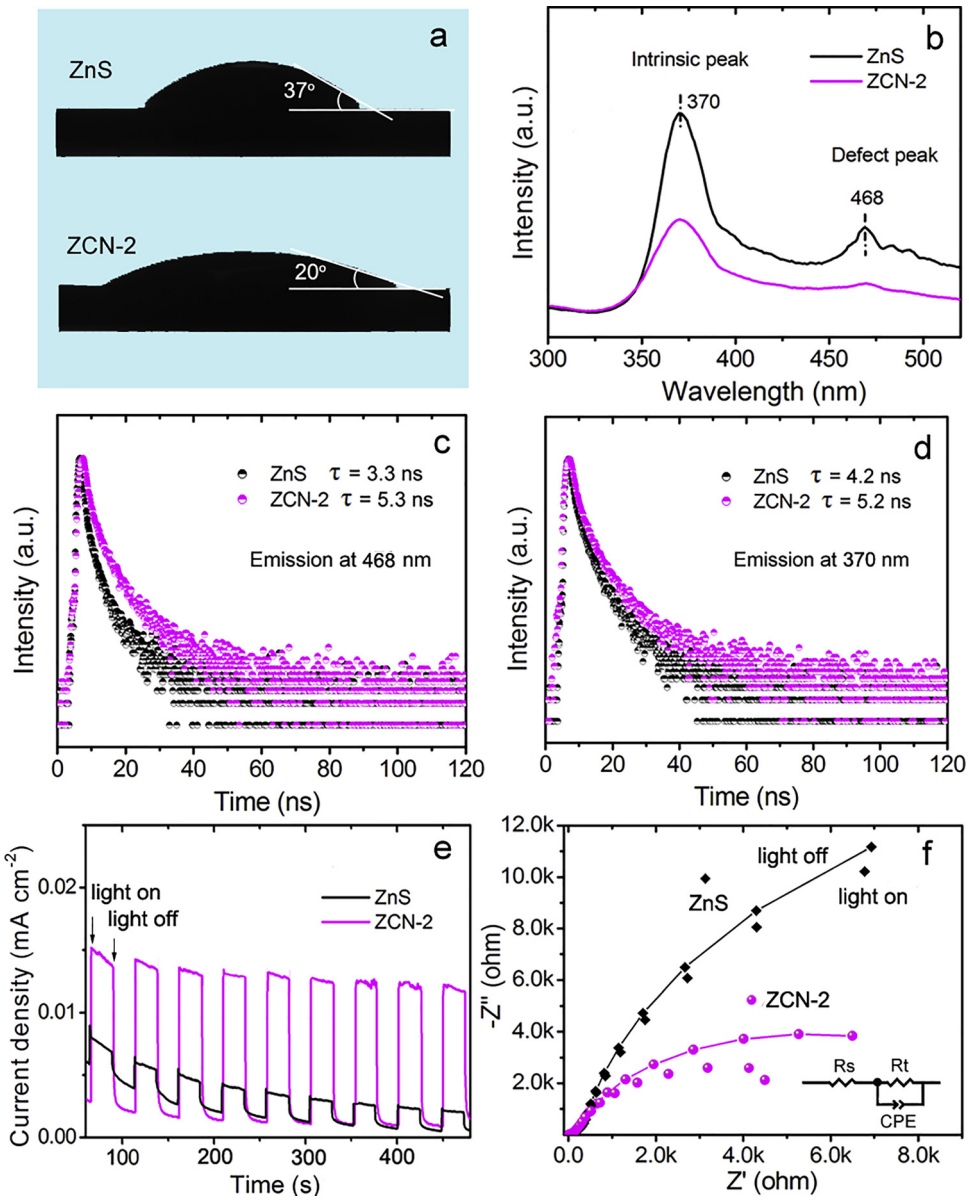

Fig. 4. (a) The hydrophily of ZnS and ZCN-2 using contact angle measurements, indicating better hydrophily of ZCN-2 than ZnS; (b) PL spectra, and (c,d) time-resolved fluorescence decay curves of ZnS and ZCN-2 with the emission wavelength of 468 nm and 370 nm; (e) Transient photocurrent density, and (f) EIS curves of ZnS and ZCN-2 with 300 W Xe light on and off (measured at 1 V vs. SCE in 0.5 M Na_2SO_4 aqueous solution). The results indicate that the carriers' separation and transfer rate of ZCN-2 are greatly improved than ZnS, and the Zn defect sites are largely passivated by the introduction of g-C_3N_4 NPs.

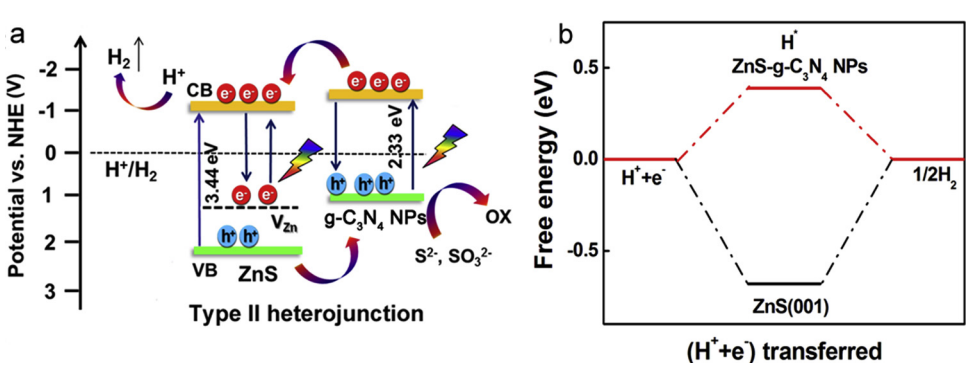

Scheme 1. (a) The photocatalytic H_2 production mechanism of the ZCN-2 photocatalyst under 300 W Xe light irradiation based on the type II heterojunction, (b) H adsorption free energy profiles of ZnS and ZCN-X, indicating the ZCN-X heterojunction introduces a non-equilibrium stoichiometry to allow a favorable hydrogen adsorption.

−COOH, −C=O, −Cl, -Br, etc. can also be introduced once changing the reaction conditions so as to further narrow the bandgap and design more desirable photocatalysts with excellent photocatalytic activity. In addition, there are many other meaningful materials that can be combined with g-C_3N_4 NPs to achieve more outstanding photocatalysts, such as carbon dots, TiO_2, and transition metal compounds, etc. Therefore, this method appears promising to prepare g-C_3N_4 NPs-related photocatalysts applied in photocatalytic fields.

5. Conclusions

In summary, -OH modified 0D g-C_3N_4 NPs with reduced dimension (within 20 nm), narrowed bandgap (2.3 eV), high reduction potential (E_{CB} = -1.03 V) are obtained via a direct hydrothermal method without using any etching agents, which is simpler, more cost effective, requires fewer reagents, and avoids harmful ultrasound compared with other techniques, showing special advantages in the application of photocatalysis. The ZCN-2 photocatalyst present a desired HER activity (5.6 mmol h^{-1} g^{-1}) under visible light, based on the enhanced surface area, shorter charge-to-surface diffusion length, fewer defect sites and accelerated carriers' separation and transfer ability. This appears to be a very promising approach toward high efficient photocatalysts and should be broadly applicable to other g-C_3N_4 NPs composites, where the low utility of sun light, particle aggregation and fast recombination of carriers hinder the widespread use of these technologies.

Acknowledgments

This work was supported by the NSFC (21574018, 51433003, 251725204, 51572179, 21471106, 21771132, and 21501126), Collaborative Innovation Center of Suzhou Nano Science & Technology, the Priority Academic Program Development of Jiangsu Higher Education Institutions (PAPD), the 111 Project, the Natural Science Foundation of Jiangsu Province (BK20161216), Jilin Provincial Education Department (543), and Jilin Provincial Key Laboratory of Advanced Energy Materials (Northeast Normal University).

Appendix A. Supplementary data

Supplementary material related to this article can be found, in the online version, at doi:https://doi.org/10.1016/j.apcatb.2018.11.054.

References

[1] C.W. Dong, S.Y. Lu, S.Y. Yao, R. Ge, Z.D. Wang, Z. Wang, P.F. An, Y. Liu, B. Yang, H. Zhang, Colloidal synthesis of ultrathin monoclinic $BiVO_4$ nanosheets for Z-scheme overall water splitting under visible light, ACS Catal. 8 (2018) 8649–8658.
[2] G. Zhou, X.Y. Xu, J.Y. Yu, B. Feng, Y. Zhang, J.G. Hu, Y.X. Zhou, Vertically aligned MoS_2/MoO_x heterojunction nanosheets for enhanced visible-light photocatalytic activity and photostability, CrystEngComm 16 (2014) 9025–9032.
[3] J. Liu, Y. Liu, N. Liu, Y. Han, X. Zhang, H. Huang, Y. Lifshitz, S.T. Lee, J. Zhong, Z.H. Kang, Metal-free efficient photocatalyst for stable visible water splitting via a two-electron pathway, Science 347 (2015) 970–974.
[4] X. Lin, D. Xu, R. Zhao, Y. Xi, L.N. Zhao, M.S. Song, H.J. Zhai, G.B. Che, L.M. Chang, Highly efficient photocatalytic activity of g-C_3N_4 quantum dots (CNQDs)/Ag/Bi_2MoO_6 nanoheterostructure under visible light, Sep. Purif. Technol. 178 (2017) 163–168.
[5] L.J. Wang, H.J. Zhai, G. Jin, X.Y. Li, C.W. Dong, H. Zhang, B. Yang, H.M. Xie, H.Z. Sun, 3D porous ZnO-SnS p-n heterojunction for visible light driven photocatalysis, Phys. Chem. Chem. Phys. 19 (2017) 16576–16585.
[6] G. Zhou, Z.J. Guo, Y. Shan, S.Y. Wu, J.L. Zhang, K. Yan, L.Z. Liu, P.K. Chu, X.L. Wu, High-efficiency hydrogen evolution from seawater using hetero-structured T/Td phase ReS_2 nanosheets with cationic vacancies, Nano Energy 55 (2019) 42–48.
[7] X.Q. Yan, M.Y. Xia, B.R. Xu, J.J. Wei, B.L. Yang, G.D. Yang, Fabrication of novel all-solid-state Z-scheme heterojunctions of 3DOM-WO_3/Pt coated by mono-or few-layered WS_2 for efficient photocatalytic decomposition performance in Vis-NIR region, Appl. Catal. B: Environ. 232 (2018) 481–491.
[8] G. Zhou, Y. Shan, Y.Y. Hu, X.Y. Xu, L.Y. Long, J.L. Zhang, J. Dai, J.H. Guo, J.C. Shen, S. Li, L.Z. Liu, X.L. Wu, Half-metallic carbon nitride nanosheets with micro grid mode 2 resonance structure for efficient photocatalytic hydrogen evolution, Nat. Commun. 9 (2018) 3366.
[9] W. Wang, J.C. Yu, Z. Shen, D.K. Chan, T. Gu, g-C_3N_4 quantum dots: direct synthesis, upconversion properties and photocatalytic application, Chem. Commun. 50 (2014) 10148–10150.
[10] G. Li, Z. Lian, W. Wang, D. Zhang, H. Li, Nanotube-confinement induced size-controllable g-C_3N_4 quantum dots modified single-crystalline TiO_2 nanotube arrays for stable synergetic photoelectrocatalysis, Nano Energy 19 (2016) 446–454.
[11] C. Xue, H. Li, H. An, B.L. Yang, J.J. Wei, G.D. Yang, NiSx quantum dots accelerate electron transfer in $Cd_{0.8}Zn_{0.2}S$ photocatalytic system via an rGO nanosheet "Bridge" toward visible-light-driven hydrogen evolution, ACS Catal. 8 (2018) 1532–1545.
[12] B.L.H. Li, H. An, W.B. Hao, J.J. Wei, Y.Z. Dai, C.S. Ma, G.D. Yang, Preparation of 2D/2D g-C_3N_4 nanosheet@$ZnIn_2S_4$ nanoleaf heterojunctions with well-designed high-speed charge transfer nanochannels towards high-efficiency photocatalytic hydrogen evolution, Appl. Catal. B: Environ. 220 (2018) 542–552.
[13] M.Y. Ye, Z.H. Zhao, Z.F. Hu, L.Q. Liu, H.M. Ji, Z.R. Shen, T.Y. Ma, 0D/2D heterojunctions of vanadate quantum dots/graphitic carbon nitride nanosheets for enhanced visible-light-driven photocatalysis, Angew. Chem. Int. Ed. 56 (2017) 8407–8411.
[14] X. Lin, D. Xu, J. Zheng, M.S. Song, G.B. Che, Y.S. Wang, Y. Yang, L.M. Chang, Graphitic carbon nitride quantum dots loaded on leaf-like $InVO_4/BiVO_4$ nanoheterostructures with enhanced visible-light photocatalytic activity, J. Alloy Compd. 688 (2016) 891–898.
[15] S. Zhang, J. Li, M. Zeng, J. Xu, X. Wang, W. Hu, Polymer nanodots of graphitic carbon nitride as effective fluorescent probes for the detection of Fe^{3+} and Cu^{2+} ions, Nanoscale 6 (2014) 4157–4162.
[16] D. Kandi, S. Martha, K.M. Parida, Quantum dots as enhancer in photocatalytic hydrogen evolution: a review, Int. J. Hydrogen Energy 42 (2017) 9467–9481.
[17] K.L. Corp, C.W. Schlenker, Ultrafast spectroscopy reveals electron-transfer cascade that improves hydrogen evolution with carbon nitride photocatalysts, J. Am. Chem. Soc. 139 (2017) 7904–7912.
[18] F. Liu, N.D. Feng, Q. Wang, J. Xu, G.D. Qi, C. Wang, F. Deng, Transfer channel of photoinduced holes on a TiO_2 surface as revealed by solid-state nuclear magnetic resonance and electron spin resonance spectroscopy, J. Am. Chem. Soc. 139 (2017) 10020–10028.
[19] J. Ren, S.X. Ouyang, H. Xu, X.G. Meng, T. Wang, D.F. Wang, J.H. Ye, Targeting activation of CO_2 and H_2 over Ru-loaded ultrathin layered double hydroxides to achieve efficient photothermal CO_2 methanation in flow-type system, Adv. Energy Mater. 7 (2017) 1601657.
[20] Y.P. Xie, Z.B. Yu, G. Liu, X.L. Ma, H.M. Cheng, CdS-mesoporous ZnS core-shell particles for efficient and stable photocatalytic hydrogen evolution under visible light, Energy Environ. Sci. 7 (2014) 1895–1901.
[21] X. Wang, G. Sun, N. Li, P. Quantum dots derived from two-dimensional materials and their applications for catalysis and energy, Chem. Soc. Rev. 45 (2016) 2239–2262.
[22] M.J. Guittet, J.P. Crocombette, M. Gautier-Soyer, Bonding and XPS chemical shifts in $ZrSiO_4$ versus SiO_2 and ZrO_2: charge transfer and electrostatic effects, Phys. Rev. B 63 (2001) 125117.
[23] K. Artyushkova, B. Kiefer, B. Halevi, A. Knop-Gericke, R. Schlogl, P. Atanassov, Density functional theory calculations of XPS binding energy shift for nitrogen-containing graphene-like structures, Chem. Commun. 49 (2013) 2539–2541.
[24] L.S. Panchakarla, K.S. Subrahmanyam, S.K. Saha, G. Achutharao, H.R. Krishnamurthy, U.V. Waghmare, C.N.R. Rao, Synthesis, structure, and properties of boron- and nitrogen-doped grapheme, Adv. Mater. 21 (2009) 4726–4730.
[25] A.K. Cuentas-Gallegos, S. López-Cortina, T. Brousse, D. Pacheco-Catalán, E. Fuentes-Quezada, H. Mosqueda, G. Orozco-Gamboa, Electrochemical study of H_3PMo_{12} retention on Vulcan carbon grafted with NH_2 and OH groups, J. Solid State Electrochem 20 (2016) 67–79.
[26] Q.C. He, F. Zhou, S. Zhan, N.B. Huang, Y. Tian, Photoassisted oxygen reduction reaction on mpg-C_3N_4: The effects of elements doping on the performance of ORR, Appl. Surf. Sci. 430 (2018) 325–334.
[27] B. Jürgens, E. Irran, J. Senker, P. Kroll, H. Müller, W. Schnick, Melem (2, 5, 8-triamino-tri-s-triazine), an important intermediate during condensation of melamine rings to graphitic carbon nitride: synthesis, structure determination by X-ray powder diffractometry, solid-state NMR, and theoretical studies, J. Am. Chem. Soc. 125 (2003) 10288.
[28] V.W. Lau, I. Moudrakovski, T. Botari, S. Weinberger, M.B. Mesch, V. Duppel, J. Senker, V. Blum, B.V. Lotsch, Rational design of carbon nitride photocatalysts by identification of cyanamide defects as catalytically relevant sites, Nat. Commun. 7 (2016) 12165.
[29] Z. Hong, B. Shen, Y. Chen, B. Lin, B. Gao, Enhancement of photocatalytic H_2 evolution over nitrogen-deficient graphitic carbon nitride, J. Mater. Chem. A 38 (2013) 11754–11761.
[30] Z.B. Fang, S.X. Weng, X.X. Ye, W.H. Feng, Z.Y. Zheng, M.L. Lu, S. Lin, X.Z. Fu, P. Liu, Defect engineering and phase junction architecture of wide-bandgap ZnS for conflicting visible light activity in photocatalytic H_2 evolution, ACS Appl. Mater. Interfaces 7 (2015) 13915–13924.
[31] P. Suyana, K.R. Sneha, B.N. Nair, V. Karunakaran, A.P. Mohamed, K.G.K. Warriera, U.S. Hareesh, A facile one pot synthetic approach for C_3N_4-ZnS composite interfaces as heterojunctions for sunlight-induced multifunctional photocatalytic applications, RSC Adv. 6 (2016) 17800–17809.
[32] H.D. Meyer, G.A. Worth, Quantum molecular dynamics: propagating wavepackets and density operators using the multiconfiguration time-dependent Hartree method, Theor. Chem. Acc. 109 (2003) 251–267.
[33] A.D. MackerellJr, M. Feig, C.L. Brooks, Extending the treatment of backbone energetics in protein force fields: limitations of gas-phase quantum mechanics in reproducing protein conformational distributions in molecular dynamics simulations, J. Computat. Chem. 25 (2004) 1400–1415.

[34] Z. Guo, U. Mohanty, J. Noehre, T.K. Sawyer, W. Sherman, G. Krilov, Probing the α-helical structural stability of stapled p53 peptides: molecular dynamics simulations and analysis, Chem. Boil. Drug Des. 75 (2010) 348–359.
[35] I. Papailias, N. Todorova, T. Giannakopoulou, N. Ioannidis, N. Boukos, C.P. Athanasekou, C. Trapalis, Chemical vs thermal exfoliation of g-C_3N_4 for NO_x removal under visible light irradiation, Appl. Catal. B: Environ. 239 (2018) 16–26.
[36] X. Wang, G. Sun, N. Li, P. Chen, Quantum dots derived from two-dimensional materials and their applications for catalysis and energy, Chem. Soc. Rev. 45 (2016) 2239–2262.
[37] R. Malik, D. Burch, M. Bazant, C. Gerbrand, Particle size dependence of the ionic diffusivity, Nano Lett. 10 (2010) 4123–4127.
[38] H.J. Yu, R. Shi, Y.X. Zhao, T. Bian, Y.F. Zhao, C. Zhou, G.I.N. Waterhouse, L.Z. Wu, C.H. Tung, T.R. Zhang, Alkali-assisted synthesis of nitrogen deficient graphitic carbon nitride with tunable band structures for efficient visible-light-driven hydrogen evolution, Adv. Mater. (2017) 1605148.
[39] H. Yaghoubi, Z. Li, Y. Chen, H.T. Ngo, V.R. Bhethanabotla, B. Joseph, S.Q. Ma, R. Schlaf, A. Takshi, Toward a visible light-driven photocatalyst: the effect of midgap-states-induced energy gap of undoped TiO_2 nanoparticles, ACS Catal. 5 (2014) 327–335.
[40] W. Yu, D. Xu, T. Peng, Enhanced photocatalytic activity of g-C3N_4 for selective CO_2 reduction to CH3OH via facile coupling of ZnO: a direct Z-scheme mechanism, J. Mater. Chem. A 3 (2015) 19936–19947.
[41] S. Ruccolo, W. Sattler, Y. Rong, P. Gerard, Modulation of Zn-C bond lengths induced by ligand architecture in zinc carbatrane compounds, J. Am. Chem. Soc. 138 (2016) 14542–14545.
[42] R.W. Gable, B.F. Hoskins, R. Robson, A new type of interpenetration involving enmeshed independent square grid sheets. The structure of diaquabis-(4, 4′-bipyridine) zinc hexafluorosilicate, J. Chem. Soc. Chem. Commun. 23 (1990) 1677–1678.
[43] W.K. Bae, L.A. Padilha, Y.S. Park, H. McDaniel, I. Robel, J.M. Pietryga, V.I. Klimov, Controlled alloying of the core-shell interface in CdSe/CdS quantum dots for suppression of Auger recombination, ACS Nano 7 (2013) 3411–3419.
[44] G. Zhou, X.Y. Xu, T. Ding, B. Feng, Z.J. Bao, J.G. Hu, Well-steered charge-carrier transfer in 3D branched Cu_xO/ZnO@Au heterostructures for efficient photocatalytic hydrogen evolution, ACS Appl. Mater. Interfaces 7 (2015) 26819–26827.
[45] L. Yao, D. Wei, Y. Ni, D. Yan, C. Hu, Surface localization of CdZnS quantum dots onto 2D g-C_3N_4 ultrathin microribbons: highly efficient visible light-induced H_2-generation, Nano Energy 26 (2016) 248–256.
[46] B. Yin, S. Zhang, Y. Jiao, Y. Liu, F. Qu, X. Wu, Facile synthesis of ultralong MnO_2 nanowires as high performance supercapacitor electrodes and photocatalysts with enhanced photocatalytic activities, CrystEngComm 16 (2014) 9999–10005.
[47] N.T. Choudhary, C. Li, J.L. Moore, N. Nagaiah, L. Zhai, Y. Jung, J. Thomas, Asymmetric supercapacitor electrodes and devices, Adv. Mater. 29 (2017) 1605336.